

Hanbury Brown and Twiss measurements in curved space

Vincent H. Schultheiss, Sascha Batz, and Ulf Peschel

In the following we will make use of $\sigma = \text{sgn}(K)$. We define $\sin_\sigma(x)$, $\cos_\sigma(x)$ and $\tan_\sigma(x)$ to be the trigonometric functions $\sin(x)$, $\cos(x)$ and $\tan(x)$ for $\sigma = +1$, while for $\sigma = -1$ they stand for the hyperbolic counterparts $\sinh(x)$, $\cosh(x)$ and $\tanh(x)$.

Two-dimensional Curved Surfaces

Differential geometry on two-dimensional surfaces knows two kinds of curvature. Imagine a plane sheet of paper easily being wrapped to a cone or a cylinder (see Fig. 1a). Although starting from a flat sheet, one certainly finds the resulting geometry curved. This kind of curvature, which depends on the embedding of a manifold in three-dimensional space, is called mean curvature $H = \frac{1}{2} \left(\frac{1}{R_1} + \frac{1}{R_2} \right)$. Here $R_{1,2}$ are the principal radii of curvature in a given point of the surface. However, trying to decompose, for example, a sphere or a saddle (see Fig. 1b,c) into flat subparts bears insuperable obstacles. In fact, there isn't even the tiniest fraction of the surface that could be flattened out without distorting distances and/or angles along the process, which is well known in cartography. The responsible intrinsic feature of the surface is the Gaussian curvature $K = \frac{1}{R_1} \cdot \frac{1}{R_2}$. Its invariance to isometric transformations is stated by Gauss's *theorema egregium*.

A non-vanishing Gaussian curvature has far reaching consequences on familiar geometric concepts when compared to Euclidean space. For example, the circumference C of a circle with radius r on a surface of constant Gaussian curvature $K = \sigma/R^2$ is given by

$$C = 2\pi R \sin_\sigma \left(\frac{r}{R} \right),$$

while the sum of the interior angles θ_i of a triangle is governed by the Gauss-Bonnet theorem

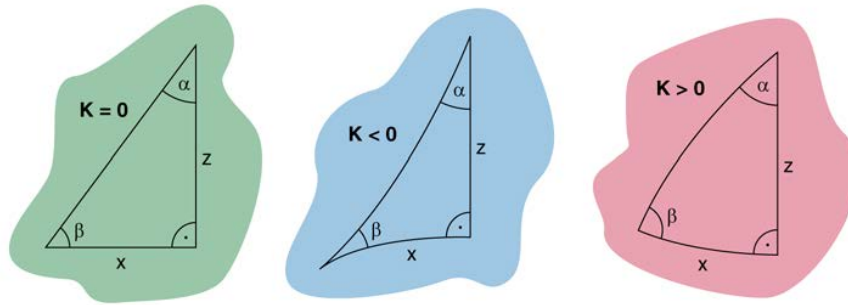
$$\sum_{i=1}^3 \theta_i = \pi + K A_{\text{triangle}},$$

where A_{triangle} is the area of the triangle. Performing either of these measurements an inhabitant of the two-dimensional curved surface can readily measure the value of the Gaussian curvature K . For a rectangular triangle made from three geodesics (see Supplementary Fig. 1) we have

$$\cos \beta = \cos_\sigma \left(\frac{z}{R} \right) \sin \alpha$$

and

$$\tan_\sigma \left(\frac{x}{R} \right) = \sin_\sigma \left(\frac{z}{R} \right) \tan \alpha.$$



Supplementary Figure 1: Sketch of rectangular triangles on curved surfaces. The sum of the interior angles depends on the value of the curvature and the enclosed area. **a)** Flat surface. **b)** Negatively curved surface. **c)** Positively curved surface.

Through the course of this paper we only deal with surfaces of revolution, because they can be fabricated conveniently. The profile curve of such a surface can be parametrised as $(r(t) \cos \varphi, r(t) \sin \varphi, h(t))$, where $r(t)$ is the distance to the axis of revolution and $h(t)$ is the height. We suppose that t is the proper length along the profile curve so that

$$\left(\frac{dr(t)}{dt}\right)^2 + \left(\frac{dh(t)}{dt}\right)^2 = 1.$$

From differential geometry it follows¹ that for surfaces of constant Gaussian curvature K

$$\frac{d^2r(t)}{dt^2} + Kr(t) = 0$$

must hold. We end up with the general solutions

$$r(t) = \begin{cases} A \cos(\sqrt{K}t) + B \sin(\sqrt{K}t) & \text{for } K > 0 \\ At + B \quad \text{with } |a| \leq 1 & \text{for } K = 0 \\ A \cosh(\sqrt{-K}t) + B \sinh(\sqrt{-K}t) & \text{for } K < 0, \end{cases}$$

from which $h(t)$ can be derived according to

$$h(t) = \int_0^t dt' \sqrt{1 - \left(\frac{dr(t')}{dt'}\right)^2}.$$

The parameters A and B can be chosen freely. Here, we set $B = 0$ so that $A = R_0$ is the radius at $t = 0$. It is important to remember, though, that the beam dynamics treated in this paper depend only on K alone, i.e., all possible surfaces of a given Gaussian curvature are equal and indistinguishable in their behaviour as long as proper lengths are used and boundary effects are negligible.

Two-dimensional Surfaces as Subspaces of Four-dimensional Spacetime

Einstein's field equations, which govern the interplay of space curvature and the mass/energy distribution in terms of general relativity, contain the Ricci tensor, the cosmological constant and a term called scalar curvature (which is the trace of the Ricci tensor). The definition and general physical significance of these geometric objects is independent of the dimensionality of the problem. In particular in the case of rotational and translational symmetry considered in this paper, the Ricci tensor is completely defined by the scalar curvature and knowledge of the latter is in fact sufficient to characterize the whole system.

The scalar curvature can be thought of as the sum of the Gaussian curvatures of two-dimensional subspaces defined by their tangent planes which are spanned by all possible pairs of base vectors. Hence, on a two-dimensional surface the scalar and the Gaussian curvature are the same up to a combinatorial factor of 2. Indeed, we can think of our two-dimensional surface embedded in three dimensional space just as a subspace of four-dimensional spacetime, which shares exactly the same properties. For example, in case of the Friedmann-Robertson-Walker metric, which describes a homogeneous and isotropic universe with constant curvature, one can show that a conveniently chosen two-dimensional subspace (time $t = \text{const.}$ and slice $\theta = \pi/2$) is completely equivalent to the two-dimensional surfaces treated in our paper in the sense that no internal observer can distinguish between the two. But taking a specific slice does not restrain generality, because the course of light evolution can only result from curvature, which is the same in every direction.

The expansion of the universe, which is also described by the Friedmann-Robertson-Walker metric, appears as a scale factor $a(t)$. It only leads to a spectral shift of the light beam, while the (wavelength dependent) dynamic of the spatial correlation stays the same.

A Short Review of Optics in Curved Space

In this section we would like to revisit the main results of Ref. 2 to clarify the conventions used in this paper. Throughout the letter we only consider rotationally symmetric macroscopic surfaces of constant Gaussian curvature K so that the mean curvature H does not affect wave propagation. In the experiments the fields propagating along the waveguides formed at the surface of the glass figures are TE-polarized, i.e., the magnetic field has only one normal component. Hence, we end up with a Helmholtz equation for that component Φ

$$k_{\text{eff}}^2 \Phi + \Delta_\gamma \Phi = 0,$$

where $k_{\text{eff}} = 2\pi n_{\text{eff}}/\lambda$ is the effective wave number of the waveguide and Δ_γ is the Laplace operator with respect to a curved two-dimensional manifold characterized by the metric γ_{ab} . In accordance to Fig. 2c,d we introduce the coordinate t as the proper length along the profile curves and the azimuthal angle φ as the transverse coordinate. On the surface of the rotational bodies used in the experiment we have the squared length element

$$ds^2 = dt^2 + R_0^2 \cos^2\left(\frac{t}{R}\right) d\varphi^2, \quad (2)$$

with the rotational body's waist radius R_0 . Hence, the Laplace operator is given by²

$$\Delta_\gamma = \partial_t^2 - \frac{\sigma}{R} \tan_\sigma \left(\frac{t}{R} \right) \partial_t + \frac{1}{R_0^2 \cos_\sigma^2 \left(\frac{t}{R} \right)} \partial_\varphi^2.$$

We now want to let a given field distribution propagate along the profile curve. For this purpose we identify the main propagation direction z with the t -direction, while $\xi = R_0\varphi$ is the transverse direction with $x = \xi \cos_\sigma(z/R)$ being the proper length in that direction (see Supplementary Fig. 2). Whereas the circles of latitude are a natural choice for the transverse coordinate on rotational surfaces, it might seem like a very specific choice and, hence, loss of generality. However, it should be pointed out that the circles of latitude are congruent with geodesics running perpendicular to the propagation direction z for small transverse distances away from the beam centre, which is consistent with the paraxial approximation.

Using the ansatz

$$\Phi(\xi, z) = \frac{1}{\sqrt{\cos_\sigma(z/R)}} u(\xi, z) e^{ik_{\text{eff}} z},$$

where the field is also rescaled, and making use of the paraxial approximation we end up with a Schrödinger equation

$$2ik_{\text{eff}} \frac{\partial u(\xi, z)}{\partial z} = -\frac{1}{\cos_\sigma^2(z/R)} \frac{\partial^2 u(\xi, z)}{\partial \xi^2} - V_{\text{eff}, \sigma}(z),$$

where

$$V_{\text{eff}, \sigma}(z) = \frac{\sigma}{4R^2} \left(1 + \frac{1}{\cos_\sigma^2(z/R)} \right)$$

is the z -dependent effective potential. This Schrödinger equation can easily be solved with standard techniques, resulting in a point spread function $h_\sigma(\xi, z)$ for the negatively and positively curved case (see Supplementary Eq. (7) below).

Although we will only focus on propagation along the profile curve in the following derivation, we could have chosen to propagate a given field distribution along any other direction as was done in the experiments shown in Fig. 3. While the solution in these cases is not straight forward, we can make use of the symmetries of our surfaces with constant Gaussian curvatures to derive the rotated solutions from the unrotated one. As was shown in Ref. 2 the rotated solution formally stays the same in the paraxial approximation that is to say for light beams narrow compared to the radius of curvature R .

A rotated set of coordinates can easily be found for any trajectory's starting point and direction by the surfaces' symmetries. Let's consider z the propagation direction in the experiment and ξ the transverse direction. For rotations around the origin by an angle α we have

$$\sin_\sigma \left(\frac{t}{R} \right) = \sin \alpha \cos_\sigma \left(\frac{z}{R} \right) \sin_\sigma \left(\frac{\xi}{R} \right) + \cos \alpha \sin_\sigma \left(\frac{z}{R} \right),$$

$$\sin_{\sigma}\left(\frac{R_0}{R}\varphi\right) = \frac{\cos\alpha \cos_{\sigma}\left(\frac{Z}{R}\right) \sin_{\sigma}\left(\frac{\xi}{R}\right) - \sin\alpha \sin_{\sigma}\left(\frac{Z}{R}\right)}{\sqrt{1 - \sigma\left(\sin\alpha \cos_{\sigma}\left(\frac{Z}{R}\right) \sin_{\sigma}\left(\frac{\xi}{R}\right) + \cos\alpha \sin_{\sigma}\left(\frac{Z}{R}\right)\right)^2}},$$

while for translations by Δt along the t -direction

$$\begin{aligned}\sin_{\sigma}\left(\frac{t}{R}\right) &= \cos_{\sigma}\left(\frac{\Delta t}{R}\right) \sin_{\sigma}\left(\frac{Z}{R}\right) - \sin_{\sigma}\left(\frac{\Delta t}{R}\right) \cos_{\sigma}\left(\frac{Z}{R}\right) \cos_{\sigma}\left(\frac{\xi}{R}\right), \\ \cos_{\sigma}\left(\frac{R_0}{R}\varphi\right) &= \frac{\cos_{\sigma}\left(\frac{\Delta t}{R}\right) \cos_{\sigma}\left(\frac{Z}{R}\right) \cos_{\sigma}\left(\frac{\xi}{R}\right) + \sigma \sin_{\sigma}\left(\frac{\Delta t}{R}\right) \sin_{\sigma}\left(\frac{Z}{R}\right)}{\sqrt{1 - \sigma\left(\cos_{\sigma}\left(\frac{\Delta t}{R}\right) \sin_{\sigma}\left(\frac{Z}{R}\right) - \sin_{\sigma}\left(\frac{\Delta t}{R}\right) \cos_{\sigma}\left(\frac{Z}{R}\right) \cos_{\sigma}\left(\frac{\xi}{R}\right)\right)^2}}.\end{aligned}$$

Since these coordinate transformations fulfil symmetry relations of surfaces with constant Gaussian curvature, they are isometric transformations, leaving the squared length element formally invariant when inserted into Supplementary Eq. (2). After the transformation the proper length in transverse direction is still given by $x = \xi \cos_{\sigma}(z/R)$.

Evolution of the Intensity Correlation

In our experiments we utilize the second order degree of coherence function $g^{(2)}(x, x')$ for optical fields E . Generally, for some transverse coordinate x

$$g^{(2)}(x, x') = \frac{\langle E(x)E(x')E^*(x')E^*(x) \rangle}{\langle E(x)E^*(x) \rangle \langle E(x')E^*(x') \rangle} = \frac{\langle I(x)I(x') \rangle}{\langle I(x) \rangle \langle I(x') \rangle}, \quad (3)$$

where $\langle \cdot \rangle$ denotes taking the mean over many phase realizations and the asterisks stand for the complex conjugates. Practically, we use (see Ref. 3)

$$g^{(2)}(\Delta x) = \frac{\langle \int dx I(x)I(x + \Delta x) \rangle}{\int dx \langle I(x) \rangle \langle I(x + \Delta x) \rangle}, \quad (4)$$

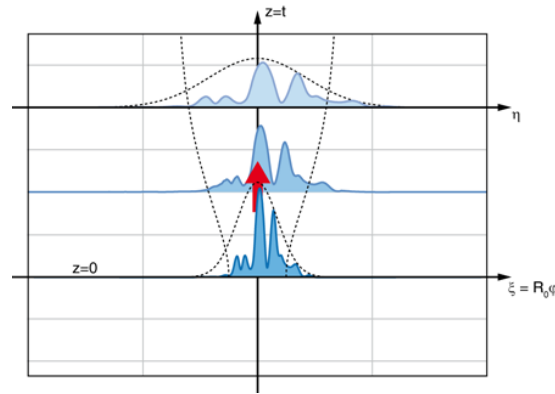
which is the mean of the intensity distributions' autocorrelations over the autocorrelation of the mean intensity distribution. This expression can be well applied in case of spatially limited field distributions. For a Gaussian correlation function like the one later described in Supplementary Eq. (8) the formulations stated in Supplementary Eqs. (3) and (4) are equivalent. Hence, for the sake of simplicity we will stick with the definition as in Supplementary Eq. (3) throughout this deviation.

Since for normally distributed fields

$$\langle I(x)I(x') \rangle = \langle I(x) \rangle \langle I(x') \rangle + |\langle E(x)E^*(x') \rangle|^2$$

holds by means of the complex Gaussian moment theorem⁴, we end up with the Siegert relation

$$g^{(2)}(x, x') = 1 + \left| \frac{\langle E(x)E^*(x') \rangle}{\sqrt{\langle E(x)E^*(x) \rangle} \sqrt{\langle E(x')E^*(x') \rangle}} \right|^2 = 1 + |g^{(1)}(x, x')|^2, \quad (5)$$



Supplementary Figure 2: Sketch of the coordinate system used to derive the speckle evolution. Every vertical line corresponds to a profile curve and every horizontal line is a circle of latitude on the rotational surface (see also Fig. 2). A spatially correlated intensity distribution with an ensemble averaged Gaussian envelope (indicated by dotted lines) propagates along the profile curve in the t -direction starting at $z = t = 0$. Our transverse coordinate at $z = 0$ is $\xi = R_0 \varphi$ (the proper length in the ξ -direction is $x = \xi \cos_\sigma(z/R)$), while after some propagation distance z the transverse coordinate shall be denoted by η to avoid ambiguousness in the convolution integral (the proper length in the η -direction is $x = \eta \cos_\sigma(z/R)$).

which relates the second order degree of coherence function to the squared modulus of the first order degree of coherence function $g^{(1)}(x, x')$. While this seems to be disadvantageous over direct measurements of the field correlation in terms of Michelson interferometry, deploying intensity measurements in astronomy generates very stable results. Even for earth-bound measurements, which are disturbed by atmospheric turbulences, no advanced stabilization techniques have to be employed⁵.

Now we want to look at the implications of Gaussian curvature on the evolution of the coherence function. Let's assume propagation along the profile curve (identifying z with the t -direction) starting at $z = 0$. Our transverse coordinate is $\xi = R_0 \varphi$, which we should keep in mind apart from $z = 0$ is not a proper length. In order to track the evolution of speckles along the propagation direction z we can make use of the point spread function (or Green's function) $h_\sigma(\xi, z)$ of the traversed optical system (or free space in that regard):

$$\langle E(\eta, z) E^*(\eta', z) \rangle = \iint d\xi d\xi' \langle E(\xi, 0) E^*(\xi', 0) \rangle h_\sigma(\xi - \eta, z) h_\sigma^*(\xi' - \eta', z), \quad (6)$$

where η shall denote the transverse coordinate after some propagation distance z to avoid ambiguousness (see Supplementary Fig. 2). The point spread function of a two-dimensional surface with constant Gaussian curvature in the paraxial approximation is given by²

$$h_\sigma(\xi, z) = \sqrt{\frac{k}{2\pi i R \sin_\sigma(z/R)}} e^{ik \frac{\xi^2}{2R \tan_\sigma(z/R)}} e^{i(k_{\text{eff}} z + \frac{1}{2k_{\text{eff}}} \int_0^z V_{\text{eff}, \sigma}(z') dz')}. \quad (7)$$

The second exponential factor of Supplementary Eq. (7) only depends on z and cancels out immediately when inserting Supplementary Eq. (7) into Supplementary Eq. (6), while the amplitude vanishes through normalization when finally calculating the second order degree of coherence function $g^{(2)}$.

Since in our experiment the speckle pattern stems from a phase modulated Gaussian laser beam, we assume the initial mutual coherence function to be described by a Gaussian Schell-model source^{6,7}

$$\langle E(\xi, 0)E^*(\xi', 0) \rangle = I_0 e^{-\frac{\xi^2 + \xi'^2}{w_0^2}} e^{-\frac{(\xi - \xi')^2}{2\rho_0^2}}. \quad (8)$$

Here w_0 is the initial field width of the Gaussian envelope and ρ_0 is the initial correlation length, since indeed by inserting Supplementary Eq. (8) into Supplementary Eq. (5)

$$g^{(2)}(\xi, \xi', z = 0) = g^{(2)}(\Delta\xi, z = 0) = 1 + e^{-\frac{\Delta\xi^2}{\rho_0^2}}.$$

where $\Delta\xi = \xi - \xi'$. For a vanishing initial correlation length ρ_0 (in the sense that ρ_0 is smaller than the resolution limit of the imaging system so that the mutual coherence function can be approximated by a delta distribution⁴) and for significant spreading of the initial field distribution Supplementary Eq. (6) qualitatively becomes a Fourier transformation of the initial intensity distribution (Van Cittert-Zernike theorem). This is why for a vanishing initial correlation length one can think of HBT measurements as examining the modulus of the initial intensity distribution's Fourier transform (which is enough for a mere size approximation). But the phase information, which is crucial for the complete reconstruction, is lost. Recently, multi-detector measurement schemes have been put forward⁸: computing the intensity correlation in a loop-like fashion (the so-called closure phase) reveals increasingly more information about the phase with every additional detector and, hence, the initial intensity distribution's symmetry. In our experiment we only consider an ensemble averaged Gaussian distribution, so the first order degree of coherence function and, thus, the interferometric visibility is real-valued.

Inserting Supplementary Eqs. (6), (7) and (8) into Supplementary Eq. (5), after some straightforward calculation and as a last step by setting

$$\Delta\eta \cos_\sigma\left(\frac{z}{R}\right) = \Delta x,$$

we eventually arrive at Eqs. (3), (4) and (5). These expressions summarize the exponential gain and the oscillation of the correlation length $\rho(z)$ during propagation on the negatively and positively curved surface, respectively. For the positively curved surface the amplitude and particularly the phase of the oscillation is governed by the ratio between the speckle diffraction length $z_S = \pi w_0^2 n_{\text{eff}} / \left(\lambda \sqrt{1 + \frac{w_0^2}{\rho_0^2}} \right)$ and the mean radius of curvature $R = 1/\sqrt{|K|}$. Note that in order to conform to the paraxial approximation in the experiments the initial Gaussian envelope width w_0 must be distinctly smaller than half the sphere's circumference, or in other words $w_0 < R$, so that figuratively speaking the field distribution is transversally localized during the propagation along the half sphere and does not interfere with itself. Consequently, in the case $z_S > R$ the minimal correlation length at $z = \pi R/2$ does not become smaller than the wavelength λ .

For $z_S = R$ the correlation length $\rho(z)$ remains unchanged during propagation (see Fig. 4d). There exists a static correlation length ρ_{stat} for every envelope field width $w_0 > \sqrt{R\lambda/\pi n_{\text{eff}}}$ (in accordance to Ref. 2). This means that the focusing of a Gaussian beam on a positively curved surface can be suppressed by implementing a finitely correlated phase shift with correlation length ρ_{stat} onto the

Gaussian envelope, leading to a static average field width $\langle w(z) \rangle = w_0$. For decreasing envelope field width this static correlation length eventually surpasses w_0 and tends to infinity.

We close by noting that in every case the ratio of the z -dependent width of the field envelope $w(z)$ and the correlation length $\rho(z)$ is constant during propagation

$$w(z)/\rho(z) = w_0/\rho_0 .$$

Therefore, the evolution of the Gaussian field envelope is determined not only by its initial width w_0 as in the case of a spatially coherent Gaussian, but also by the initial correlation length ρ_0 . This can be seen as a generalisation of the results derived in Ref. 2 for incoherent field distributions.

Evolution of the Correlation Length in Terms of Length Measurements on the Surface

To extract the actual size of the light source from measuring the transverse correlation length we have to know its proper distance from the observation plane. For an observer living inside the two-dimensional curved surface the latter might not be ascertainable directly, which has forced, e.g., astronomers to deploy alternate measurement schemes. In this section we want to exemplarily discuss the replacement of the proper distance z in Eqs. (4) and (5) by more accessible distance measures accepted in astronomy, which both have in common that their utilization disguises the characteristic exponential and oscillatory behaviour of negatively and positively curved space, respectively.

a) Apparent brightness as a distance measure

The apparent brightness (or energy flux) b of a source with luminosity L inside the surface scales inversely to the circumference C of a circle with radius z around the source (see Fig. 1) so that

$$R \sin_\sigma \left(\frac{z}{R} \right) = \frac{L}{2\pi b} \quad (9)$$

holds. We define the right-hand side as our new effective distance measure d_{eff} . By inserting this expression into Eqs. (4) and (5) the characteristic dynamics of curved space are lost (see Eq. (6)) underlining the importance of the choice of reference parameters.

It should be pointed out that in the limit $\rho_0 \rightarrow 0$ (in the sense described on page 7) we arrive at

$$\rho(d_{\text{eff}}) = \frac{\lambda}{\pi w_0} d_{\text{eff}} = \frac{\lambda}{\pi \theta} ,$$

where θ is the angular size of the source as observed by an inhabitant of the curved space in accordance with Supplementary Eq. (1) for $w_0 \ll R$ and $\theta \lesssim 1$.

b) Parallax as a distance measure

The parallax is defined as the opening angle of a geodesic triangle (α in Supplementary Fig. 1) under which the orbital diameter of earth on its way around the sun is visible. In flat space this angle α is

identical to the angle of a star's apparent movement in front of the fixed background stars due to the two being alternate interior angles. In practice, this is exactly how measurements are performed. In curved space, however, the angle of apparent movement visible from earth is not identical with the opening angle anymore and the relation becomes rather complicated.

Here we want to look at an inverted parallax measurement with the observer sitting at the corner opposite to the baseline x , since only for an inverted triangle we find a relation which is capable of disguising the dynamics of curved space again. The feasibility of inverted parallax measurements in astronomy was shown just recently⁹ and similar measurements even allow for an estimation of the universe's curvature from the angular structure of the cosmic microwave background¹⁰. From Supplementary Eq. (1) for $x \ll R$ and accordingly $\alpha \lesssim 1$ we find

$$R \sin_{\sigma} \left(\frac{z}{R} \right) \approx \frac{x}{\tan \alpha} \approx \frac{x}{\alpha}.$$

Once more, using the right-hand side as our new effective distance measure d_{eff} and inserting this expression into Eq. (4) and (5) the dynamics of the evolution of the correlation function are lost.

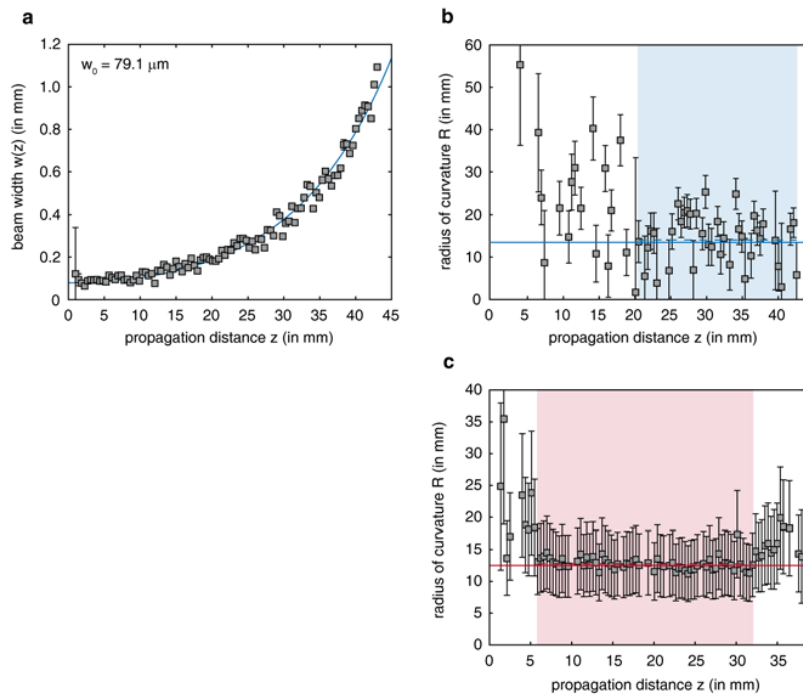
Reconstruction of the Gaussian Curvature from Correlation Measurements

While the knowledge of proper distances in the experiment immediately enables us to fit or calculate the source's original size and/or the surface's intrinsic curvature from respective experimental data, this information might not be directly available, but has to be concluded from other measures such as the apparent brightness of the light source (see previous section). Here we'd like to shortly summarize the scheme to derive the value of the Gaussian curvature K from comparing the evolution of two different sources after the same propagation distance. The two sources might differ in any of the initial parameters (initial width w_0 , initial correlation length ρ_0 , wavelength λ) and may even implement the limiting cases of vanishing or infinite initial correlation length. By equating the expressions for $\rho(z)$ and $\rho'(z)$, representing the two sources, we get

$$K = \frac{1}{z_S^2 z'_S} \frac{z_S^2 \left(\frac{\rho(z)^2}{\rho_0^2} - 1 \right) - z'_S{}^2 \left(\frac{\rho'(z)^2}{\rho_0'^2} - 1 \right)}{\left(\frac{\rho(z)^2}{\rho_0^2} - 1 \right) - \left(\frac{\rho'(z)^2}{\rho_0'^2} - 1 \right)}, \quad (10)$$

from which $R = 1/\sqrt{|K|}$ can readily be calculated. If a source has an infinite initial correlation length the respective terms in Supplementary Eq. (10) must be exchanged with the characteristic values of a homogeneous Gaussian beam, i.e., $\rho'(z)$ becomes $w'(z)$, ρ'_0 becomes w'_0 and the speckle diffraction length z'_S turns into the Rayleigh length z'_R .

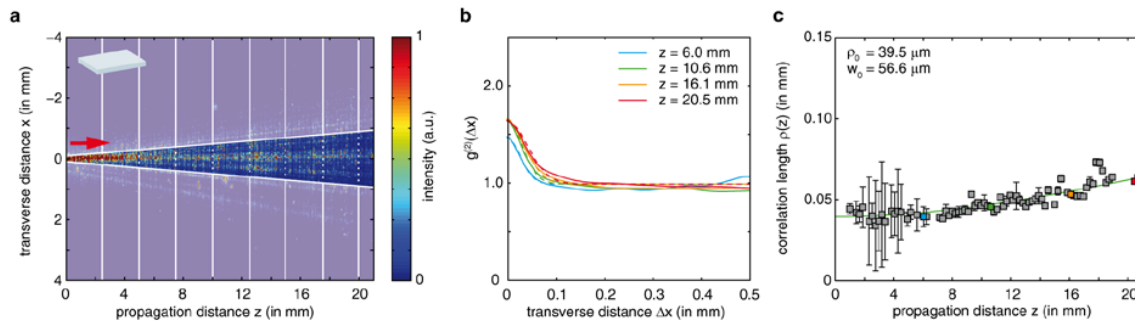
To underline this point we will use two different approaches to extract the radii of curvature of the negatively and positively curved surfaces. In case of the hourglass-type figure we utilize the measurement for a finite initial correlation length depicted in Fig. 3c and performed an additional measurement to track the evolution of the envelope width of a homogeneous, i.e., infinitely correlated Gaussian beam¹¹ (see Supplementary Fig. 3a). In case of the half-sphere we compare the two data sets displayed in Fig. 3f and i, which drastically differ in their initial values as much as they have a phase shift of $\pi R/2$ in their oscillatory behaviour.



Supplementary Figure 3: Measurement of the radius of curvature from correlation data. Two different sets of measurements are needed in order to calculate the radius of curvature R without explicit knowledge of the distance z to the light source. **a)** Evolution of the beam width $w(z)$ of a homogenous Gaussian beam on the negatively curved surface. **b)** Calculated radius of curvature R for every propagation distance z utilizing the Gaussian width displayed in subfigure a) and the data set displayed in Fig. 3c). The values converge for large propagation distances as the experimentally determined correlation lengths are well above the resolution limit. The solid blue line represents the actual radius of curvature of the hourglass-like figure $R_{K<0} = 13.5$ mm, the dashed blue line is the result of a constant fit in the shaded interval $R_{\text{exp}, K<0} = 14.1 \pm 1.1$ mm. **c)** Calculated radius of curvature R for every propagation distance z utilizing the two data sets depicted in Fig. 3f) and i) of the main paper. Again, values originating from very small correlation lengths are to be neglected. The solid red line represents the actual radius of curvature of the half-sphere $R_{K>0} = 12.5$ mm, while the dashed red line is the result of a constant fit in the shaded interval $R_{\text{exp}, K>0} = 12.8 \pm 0.1$ mm.

The end results are illustrated in Supplementary Fig. 3b and c. The calculated values converge well for large experimentally determined correlation lengths fairly above the resolution limit of the experiment. For the hourglass figure the errors are mainly due to experimental uncertainties in the retrieval of $\rho(z)$ and $w'(z)$. For the half-sphere the variation of the calculated values is very small, which might seem surprising considering the deviations of the correlation lengths from the theoretical curves as visible in Fig. 3f and i. However, Supplementary Eq. (10) is only governed by the speckle diffraction lengths and the *relative* evolution of the correlation lengths with respect to their initial values. The larger values dominate the calculation so that in our case for small propagation lengths the result is mostly determined by Fig. 3i and for propagation lengths around $\pi R/2$ the result is mostly determined by Fig. 3f. This way the disadvantages of both measurements are evening out. The errors depicted in Supplementary Fig. 3c are mainly due to uncertainties in the initial correlation length ρ_0 and width w_0 and, hence, of systematic nature.

We find $R_{\text{exp}, K<0} = 14.1 \text{ mm} \pm 1.1 \text{ mm}$ for the hourglass-type figure, which is in very good accordance with the surface's actual radius of curvature $R_{K<0} = 13.5 \text{ mm}$, and $R_{\text{exp}, K>0} = 12.8 \text{ mm} \pm 0.1 \text{ mm}$ for the half-sphere, compared to its actual value $R_{K>0} = 12.5 \text{ mm}$. (The error stated is the error of the fit parameter.)



Supplementary Figure 4: Measurement of the second order DOC function on a flat reference. **a)** Realization of a speckle distribution. The beam is coupled on the left side and propagates to the right. Framing white lines limit the central region used in the evaluation. Vertical white lines represent geodesics perpendicular to the propagation direction. **b)** Correlation function $g^{(2)}(\Delta x)$ for four different propagation lengths. The different colours correspond to the coloured squares in subfigure c). Solid lines are experimental measurements and dashed lines represent Gaussian fits. The deviation of $g^{(2)}(0)$ from 2 is due to an insufficient signal-to-noise ratio in the CCD camera as well as the finite scatterer and CCD pixel size. **c)** Evolution of the correlation length as extracted from Gaussian fits. Error bars show the fit parameter's confidence interval. The green line is a fit with Eq. (4) in the limiting case of an infinite radius of curvature R .

Experimental Evaluation of the Second Order Degree of Coherence Function in Flat Space

For reference, in Supplementary Fig. 4 we show measurements on a flat substrate with a waveguide identical to the one realized along the negatively curved surface. The flat crown glass specimen was present in the hot melt together with the hourglass-type figure during the ion exchange process (see method section) and, hence, their waveguiding layers share the same properties. The second order degree of coherence function was built from 1000 phase realizations. The results are in good agreement with the flat limit of Eqs. (4) or (5).

Impact of a Resolution Limit on the Correlation Function

Since the glass imperfections, which scatter light from the curved surfaces to the CCD camera, and the CCD pixels themselves have a certain spatial extent, they both impose a limit to the experimental resolution of spatial intensity variations and, thus, the measurable correlation length. In Supplementary Fig. 5 we have plotted in bigger size sample measurements of the evolution of spatially incoherent beams along the negatively and positively curved surfaces. These images are accompanied by exemplary intensity distributions as obtained in our experiment. The pixel size is about 50 μm in each case. The scatterer size is of the same order.

In the following we will analyse the implications of a coarse resolution on the second order DOC function $g^{(2)}(\Delta x)$. To this end we consider a pixelation of the intensity distribution as a simple model for both the CCD pixels and the scatterers. We start by noting that the intensity $I(x)$ is constant over one pixel

$$I(x) = \int_{n\delta x}^{(n+1)\delta x} dx' I(x') ,$$

where δx is the pixel size and $n = \text{floor}(x/\delta x)$ is an integer. Inserting this into Supplementary Eq. (4) and rearranging the integrals we arrive at

$$g^{(2)}(\Delta n \delta x) = \frac{\sum_n \int_n^{(n+1)\delta x} dx' \int_{(n+\Delta n)\delta x}^{(n+\Delta n+1)\delta x} dx'' \langle I(x') I(x'') \rangle}{\sum_n \int_n^{(n+1)\delta x} dx' \int_{(n+\Delta n)\delta x}^{(n+\Delta n+1)\delta x} dx'' \langle I(x') \rangle \langle I(x'') \rangle}.$$

Here we assumed that due to the resolution limit we evaluate the second order DOC function only at steps $\Delta n = \Delta x/\delta x \in \mathbb{N}$. Supposing a random field distribution with uniform envelope and mutual coherence function

$$\langle E(x') E^*(x'') \rangle = I_0 e^{-\frac{(x'-x'')^2}{2\rho^2}}$$

we find following the Siegert relation

$$\langle I(x') I(x'') \rangle = I_0^2 \left(1 + e^{-\frac{(x'-x'')^2}{\rho^2}} \right)$$

with $I_0 = \langle I(x') \rangle = \langle I(x'') \rangle$. Calculating the integrals and sums we end up with an analytic expression for the course of the second order DOC function

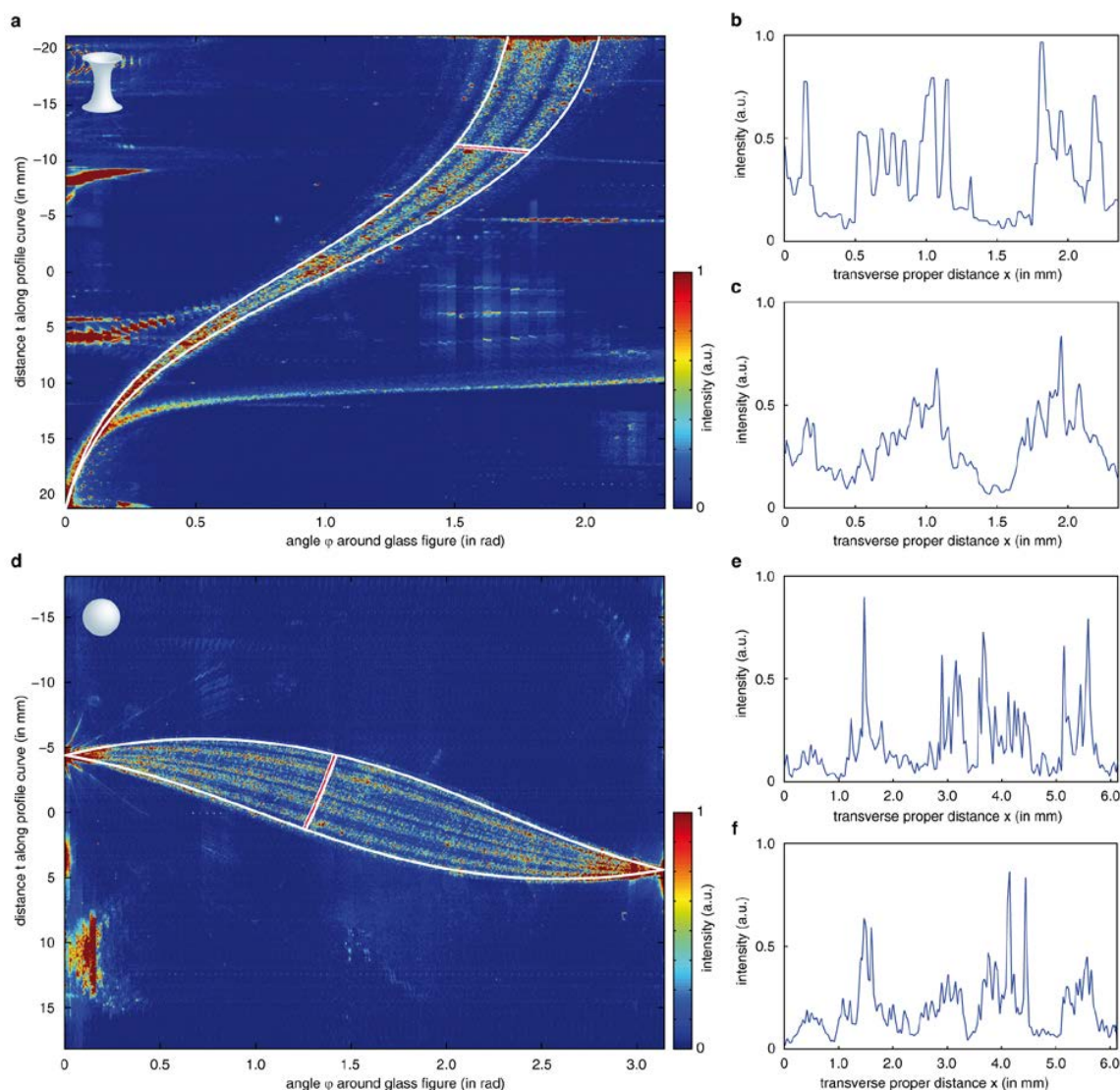
$$g^{(2)}(\Delta n) = 1 + \frac{a^2}{2} \left(e^{-\frac{(\Delta n-1)^2}{a^2}} - 2e^{-\frac{\Delta n^2}{a^2}} + e^{-\frac{(\Delta n+1)^2}{a^2}} \right) + \frac{a\sqrt{\pi}}{2} \left[(\Delta n-1) \text{erf}\left(\frac{\Delta n-1}{a}\right) - 2\Delta n \text{erf}\left(\frac{\Delta n}{a}\right) + (\Delta n+1) \text{erf}\left(\frac{\Delta n+1}{a}\right) \right], \quad (11)$$

where $a = \rho/\delta x$ is the ratio of the correlation length and the pixel size. Of interest is also the value for vanishing transversal shift $\Delta n = 0$

$$g^{(2)}(0) = 1 - a^2 + a^2 e^{-\frac{1}{a^2}} + a\sqrt{\pi} \text{erf}\left(\frac{1}{a}\right).$$

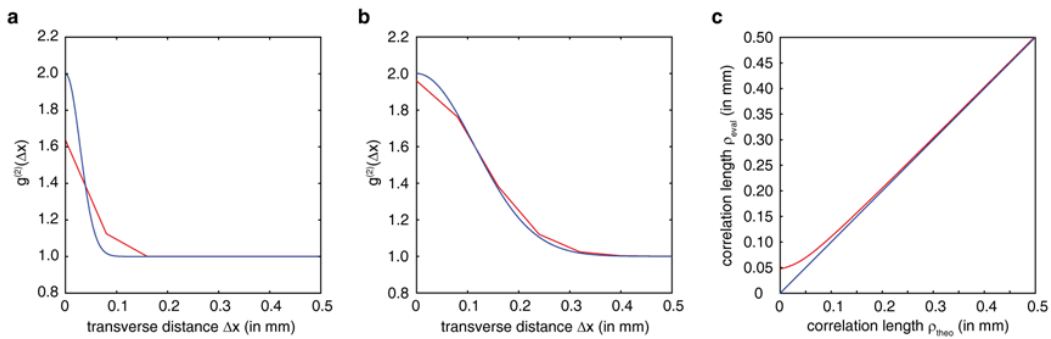
Depending on a this value actually varies between 1 and 2 in contrast to what is expected from an incoherent field distribution. In Supplementary Fig. 6 we have plotted Supplementary Eq. (11) for $\delta x = 80 \mu\text{m}$ and different values of a , as well as the correlation length ρ_{eval} as extracted from a Gaussian fit. As the correlation length surpasses the pixel size δx the second order DOC function $g^{(2)}(\Delta n)$ not only is broader than the theoretical curve, but its peak is also significantly lower than 2. Since the intensity variations cannot be resolved anymore, the field distribution appears to be more coherent than it actually is.

It should be noted that because of the Gaussian fit involved to extract the correlation length ρ_{eval} the resulting value can in fact be smaller than the pixel size δx . When the correlation drops down to almost zero over the course of one pixel, this is reasonable. Since we were still not able to measure correlation lengths smaller than the pixel size of $50 \mu\text{m}$, the size of the glass imperfections dominates the resolution limit in our experiment. If we assume our simplified model from above, $\delta x = 80 \mu\text{m}$ corresponds well to the found resolution limit as apparent in Fig. 3 of the main paper.



Supplementary Figure 5: Raw experimental data. **a)** Sample measurement of the evolution of a spatially incoherent beam on the negatively curved surface. The image is oversaturated to make details visible. One pixel corresponds to $50\ \mu\text{m}$ in each direction. For the evaluation only a central region is considered (truncated on both sides by geodesics indicated as white lines). The intensity profile along the transverse direction x is extracted at longitudinal steps of $\Delta z = 106\ \mu\text{m}$. Four such lines (three white and one red) are plotted for demonstration. **b)** Intensity distribution along the red line of subfigure a). **c)** Mean intensity distribution as obtained from all four lines. **d)** Sample measurement on the positively curved surface. The image is oversaturated to make details visible. Again the framing white lines limit the evaluation region. One pixel corresponds to $53\ \mu\text{m}$ in each direction and the intensity profile along the transverse direction x is extracted at longitudinal steps of $\Delta z = 93\ \mu\text{m}$. **e)** Intensity distribution along the red line of subfigure d). **f)** Mean intensity distribution as obtained from all four lines.

In a more realistic approach one can think of the high resolution intensity distribution being convoluted with the shape of an average scatterer, acting like a low pass filter in concealing fine intensity variations and, hence, increasing spatial correlation. Like in the case of pixelation this results in a second order DOC function which is broader than its theoretical counterpart and has a peak well beneath 2.



Supplementary Figure 6: Effect of a resolution limit on the second order DOC function. **a), b)** Depicted as a red line is the course of Supplementary Eq. (11) for $\delta x = 80 \mu\text{m}$ with **a)** $a = 0.5$ and **b)** $a = 2.0$, respectively. The blue lines represent the expected theoretical curves when no pixelation is present. For $a < 1$ the distribution is broader than the theoretical Gaussian with its peak significantly lower than 2. As a increases the distribution quickly converges to a Gaussian shape with its peak at 2. **c)** Comparison of the theoretical correlation length ρ_{theo} and the evaluated correlation length ρ_{eval} resulting from Gaussian fits to the second order DOC functions with $\delta x = 80 \mu\text{m}$ (red line) and no resolution limit (blue line).

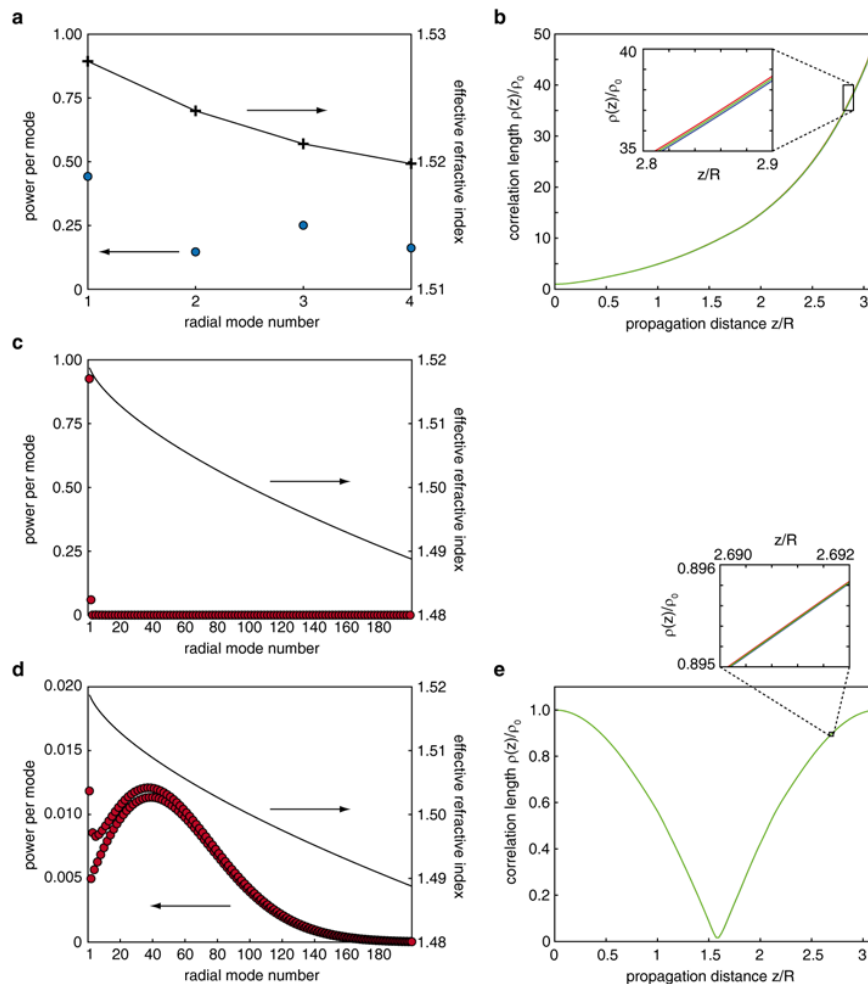
The considerations treated above represent no fundamental obstacle of the HBT scheme in curved space and can in principle be dealt with by utilizing finer stray centers or intentional structuring for advanced scattering, and by an imaging system with better resolution (larger aperture, smaller pixel size of the CCD camera chip). The resolution of the astronomic analogue measurement and its uncertainty on the other hand is governed by the telescope area and light sensitivity.

Multimode Excitation in the Experiment

a) Multimode Waveguide

As mentioned in the Method Section of the main paper a waveguiding layer was generated along the negatively curved surface by means of ion diffusion. The process was optimized for single mode operation at a wavelength $\lambda = 1550 \text{ nm}$. Since the experiments presented in this paper were performed at $\lambda = 532 \text{ nm}$, we have to investigate the impact of multimode excitation on the experimental outcome.

Assuming a refractive index modulation in the form of an error function in the direction normal to the surface and considering single mode behavior at $\lambda = 1550 \text{ nm}$, we are able to model the refractive index profile and extract all guiding waveguide modes by means of a mode solver. At $\lambda = 532 \text{ nm}$ ($n_{\text{glass}} = 1.52$) we find four TE-modes, the effective refractive indices of which differ at most by $8 \cdot 10^{-3}$. Through front face coupling a limited number of modes is excited depending of the shape and width of the impinging beam. The amount by which a certain mode is excited depends on the spatial overlap with the exciting field distribution and can be calculated with help of the overlap integral. In our experimental situation the exciting beam has a Gaussian profile of $12.6 \mu\text{m}$ normal width. The power stored in the single modes (overlap integral squared) is depicted in Supplementary Fig. 7a. Since the impinging beam is rather broad, all four modes are excited evenly.



Supplementary Figure 7: Multimode excitation. **a)** Depicted is the normalized power stored in every of the four guiding TE-modes of the waveguide along the hourglass-type figure (blue circles). The effective refractive indices span a range of $8 \cdot 10^{-3}$ as indicated by the black crosses. **b)** Results of a full set of simulations with 1000 phase realizations. The evolution of the correlation length stemming from simulations with propagation constant $k = 10000 \text{ mm}^{-1}$ (blue line) is accompanied by the results obtained for $k = 9950 \text{ mm}^{-1}$ (red line) and the results obtained for the incoherent superposition of the respective field distributions (green line). The three curves are indistinguishable within the experimental resolution limit (see also inset). **c)** Normalized power stored in the first 200 TE-polarized radial modes of the half sphere for the case $z_S < R$ (red circles). The first mode is excited almost exclusively. **d)** Normalized power stored in the first 200 TE-polarized radial modes of the half sphere for the case $z_S > R$ (red circles). The effective refractive indices of the excited modes span a range of about $3 \cdot 10^{-2}$ as indicated by the black line. **e)** Results of a full set of simulations with 1000 phase realizations for $z_S > R$. The evolution of the correlation length evaluated from simulations with propagation constant $k = 10000 \text{ mm}^{-1}$ (blue line), the results obtained for $k = 9800 \text{ mm}^{-1}$ (red line) and the results for the incoherent superposition of the field distributions (green line) are practically identical (see also inset).

It is crucial, however, to note that the guided modes form an orthogonal set of eigenfunctions and, thus, do not interfere. The intensity distribution at the surface can be treated as an incoherent superposition of the single field distributions, i.e., the sum of intensities. The evolution of the fields, though, is primarily governed by the radius of curvature R and only little by the quite equal effective refractive indices. Hence, the observable consequences are very small. This was confirmed by a full set of simulations with 1000 phase realizations and subsequent evaluation of the second order DOC function $g^{(2)}(\Delta x, z)$ for the incoherent superposition of two excited modes with propagation

constants $k = 10000 \text{ mm}^{-1}$ and $k = 9950 \text{ mm}^{-1}$ (see Fig. 4a of the main paper for the other parameters). The resulting evolution of the transverse correlation $\rho(z)$ is plotted in Supplementary Fig. 7b. No deviations from the single mode excitation above the resolution limit of our experiment are visible.

b) Radial Modes of the Sphere

Light propagating along the surface of a sphere experiences total internal reflection with respect to the outer surface. But it is also subject to a kind of centripetal force preventing the radiation from penetrating the interior of the sphere. The result is a guided mode structure with respect to the radial dimension, which has been extensively studied in the framework of whispering gallery mode (WGM) resonators^{12,13}. Similar to the waveguiding modes above, the WGMs form an effectively orthogonal set of eigenfunctions so that different modes do not interfere.

The relevance of higher mode excitation is governed by the actual experimental situation. To clarify the matter we must distinguish between the cases $z_S < R$ and $z_S > R$. In the former case the light beam was focused on the entrance facet of the glass sphere with a combination of a cylindrical lens and a microscope objective achieving a radial Gaussian width of about $5 \mu\text{m}$. Since the excitation of a radial mode is proportional to the spatial overlap with the impinging field distribution, it can be shown that in this case the fundamental mode was excited almost exclusively (see Supplementary Fig. 7c).

For $z_S > R$ the beam was prepared with a combination of cylindrical lenses to have a larger radial extent (about $200 \mu\text{m}$ in radial width with the barycenter about $100 \mu\text{m}$ from the edge) in order to be able to launch a transversally broad beam into the half sphere. Evaluation of the overlap integrals hints at a roughly uniform excitation of up to 100 modes (see Supplementary Fig. 7d). However, the effective refractive indices are very close to each other, only spanning a range of $3 \cdot 10^{-2}$, which corresponds to 2% of the refractive index of glass. Even more important, for $z_S > R$ the beam evolution is mainly governed by the radius of curvature R . The effective refractive index, which affects the beam diffraction, plays only a minor role.

We simulated a full set of 1000 phase realizations representing the sum of two intensity evolutions with propagation constants $k = 10000 \text{ mm}^{-1}$ and $k = 9800 \text{ mm}^{-1}$ (see Fig. 4c of the main paper for the other parameters). The evolution of the transverse correlation $\rho(z)$ is plotted in Supplementary Fig. 7e. It shows no deviations from the single mode excitation above the resolution limit of our experiment.

References:

1. Kühnel, W. & Hunt B. *Differential Geometry: Curves–Surfaces–Manifolds* (American Mathematical Society, Providence, 2005), 2nd edition.
2. Batz, S. & Peschel U. Linear and nonlinear optics in curved space. *Phys. Rev. A* **78**, 043821 (2008).
3. Bromberg, Y., Lahini, Y., Small, E. & Silberberg, Y. Hanbury Brown and Twiss interferometry with interacting photons. *Nature Photon.* **4**, 721-726 (2010).

4. Goodman, J. W. *Statistical Optics* (John Wiley & Sons, New York, 2000).
5. Hanbury Brown, R. & Twiss, R. Q. A test of a new type of interstellar interferometer on Sirius. *Nature* **178**, 1046-1048 (1956).
6. Foley, J. T. & Zubairy, M. S. The directionality of Gaussian Schell-model beams. *Opt. Comm.* **26**, 297-300 (1978).
7. Friberg, A. T. & Sudol, R. J. Propagation parameters of Gaussian Schell-model beams. *Opt. Comm.* **41**, 383-387 (1982).
8. Malvimat, V., Wucknitz, O. & Saha, P. Intensity interferometry with more than two detectors? *MNRAS* **437**, 798-803 (2014).
9. Hönig, S. F. *et al.* A dust-parallax distance of 19 megaparsecs to the supermassive black hole in NGC 4151. *Nature* **515**, 528-530 (2014).
10. Kamionkowski, M., Spergel, D. N. & Sugiyama, N. Small-scale cosmic microwave background anisotropies as a probe of the geometry of the universe. *Astrophys. J.* **426**, L57 (1994).
11. Schultheiss, V. H. *et al.* Optics in curved space. *Phys. Rev. Lett.* **105**, 143901 (2010).
12. Oraevsky, A. N. Whispering-gallery waves. *Quant. Electron.* **32**, 377-400 (2002).
13. Breunig, I., Sturman, B., Sedlmeir, F., Schwefel, H. G. L. & Buse, K. Whispering gallery modes at the rim of an axisymmetric optical resonator: analytical versus numerical description and comparison with experiment. *Opt. Express* **21**, 30683-30692 (2013).